REMOTE SENSING USING SPACE BASED RADAR

Braham Himed
Air Force Research Laboratory Sensors Directorate
26 Electronic Parkway Rome, NY 13441
Email: Braham.Himed@rl.af.mil

Ke Yong Li
C&P Technologies, Inc. 317 Harrington Avenue
Suites 9&10 Closter, NJ 07624
Email: kli@cptnj.com

S. Unnikrishna Pillai
Dept. of Electrical Engg. Polytechnic University
6 MetroTech Center Brooklyn, NY 11201
Email: pillai@hora.poly.edu

Abstract A Space-Based Radar (SBR) is a reconnaissance, surveillance, and target acquisition system capable of supporting a wide variety of joint missions and tasks simultaneously, including battle management, command and control, target detection and tracking, wide area surveillance and attack operations. SBR also supports traditional intelligence, surveillance and reconnaissance missions such as indications, warning, and assessment. These mission areas cover the strategic, operational, and tactical levels of operations of interest. SBR systems are also used for earth science projects. However, an SBR system, by virtue of its motion, generates a Doppler frequency component to the clutter return from any point on the earth as a function of the SBR-earth geometry. The effect of earth's rotation around its own axis is shown to add an additional component to this Doppler frequency. The overall effect of the earth's rotation on the Doppler turns out to be two correction factors in terms of a crab angle affecting the azimuth angle, and a crab magnitude scaling the Doppler magnitude of the clutter patch. Interestingly both factors depend only on the SBR orbit inclination and its latitude and not on the specific location of the clutter patch of interest. It is also shown that earth's rotation together with the range foldover phenomenon inherent in such systems; significantly degrade the clut-

ter suppression performance of adaptive processing algorithms. In this chapter, we provide analytical derivations of these phenomena and their impact on performance, and suggested ways to remedy for these effects are shown through computer simulations.

Keywords: SBR; STAP; earth rotation; range ambiguity; crab angle; crab magnitude; Doppler dispersion; range dependency; waveform diversity; Doppler warping.

1. Introduction

SBR because of its height can cover a very large area on earth for intelligence, surveillance and monitoring of ground moving targets. Once launched into orbit, the SBR moves around the earth while the earth continues to rotate on its own axis. By adjusting the SBR speed and orbit parameters, it is thus possible to scan various parts of the earth periodically and collect data. Such an SBR based surveillance system can be remotely controlled and may require very little human intervention. As a result, targets of interest can be identified and tracked in greater detail and/or images can be made with a very high resolution. In SBR systems, the range foldover phenomenon — clutter returns that correspond to previous/later radar pulses — contributes to the SBR clutter. Another important phenomenon that affects the clutter data is the effect of earth's motion around its own axis. At various points on earth this contributes differently to Doppler, and the modification to Doppler due to earth's rotation will be shown to induce a crab angle and a crab magnitude. These two components are shown to induce Doppler dispersion that is shown to be range-dependent. This range dependency causes the secondary data to be non independent and identically distributed (iid); an assumption that is required by most STAP approaches. The simultaneous presence of earth rotation and range foldover — a condition that generally applies — causes performance degradation in most STAP approaches. To mitigate these effects, we propose to use waveform diversity on transmit. Detailed performance analysis and methods that minimize these effects are given in great detail in this chapter.

2. Geometry

2.1 Radar-Earth Geometry

A space based radar (SBR) located at an orbital height H above its nadir point has its mainbeam focused to a point of interest D on the ground located at range R [1]–[4]. In general, the SBR can be in an orbit that is inclined at an angle to the equator. The inclination of

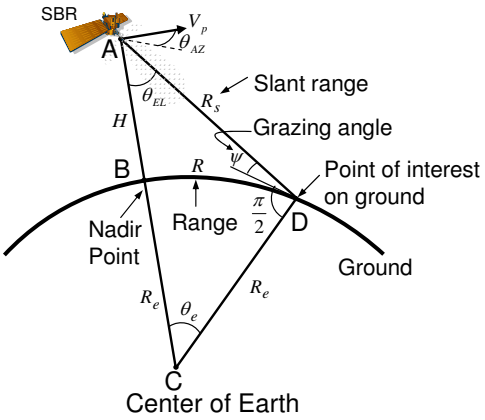

Figure 1. Parameters of an SBR pointing its mainbeam to a ground point D.

the SBR orbit is usually given at the point where it crosses the equator from which its local inclination at other latitudes can be determined. The range is measured from the nadir point B (that is directly below the satellite) to the antenna mainbeam footprint on earth (see Fig. 1). For example, a polar satellite at 506 km above the earth's surface has a period of 1.57 hours. While it completes a circle around the earth that is fixed with respect to the stars, the earth turns through 22.5^o or $1/6$ of a revolution about its axis. Thus, every time the space craft crosses the equator the earth moves 2500 km eastward giving an 'automatic' scan of the surface below to the onboard radar. As a result, the radar is able to scan the earth in both latitude and longitude by virtue of the earth's rotation.

In Fig. 1, the SBR is located at A, and B represents the nadir point. The point of interest D is located at range R from B along the great circle that goes through B and D with C representing the center of the earth (see [5]). The main parameters of an SBR setup are as shown in Fig. 1 and are listed in the table in figure 2.

From Fig. 1, the core angle subtended at the center of earth by the range arc BD is given by

$$\theta_e = R/R_e \tag{1}$$

and from triangle ACD we get

$$R_s^2 = R_e^2 + (R_e + H)^2 - 2R_e(R_e + H)\cos\,\theta_e. \tag{2}$$

Thus, the slant range R_s equals

$$R_s = \sqrt{R_e^2 + (R_e + H)^2 - 2R_e(R_e + H)\cos(R/R_e)} \quad . \tag{3}$$

R	Actual ground range from the nadir point to the point of interest along a great circle on the surface of the earth
H	SBR orbit height above the nadir point
R_s	Radar slant range from the satellite to the antenna footprint at range R
ψ	Grazing angle at the antenna footprint at range R (i.e., the angle at which the surface is illuminated by the radar beam)
R_e	Earth's radius (3,440 miles or 6,373 km)
θ_{EL}	Mainbeam elevation from the vertical line associated with range R.
θ_{AZ}	Azimuth point angle measured between the plane of the array (generally also the SBR velocity vector) and the elevation plane
V_P	Satellite velocity vector
θ_e	Core angle between the nadir point and the grazing point measured at the earth's center.

Figure 2. SBR Parameters

Similarly, the grazing angle ψ is also a function of range. To see this, referring back to the triangle ACD we have the grazing angle at range R to be

$$\psi = \cos^{-1}\left(\frac{R_e + H}{R_s}\sin\left(R/R_e\right)\right), \tag{4}$$

and the corresponding elevation angle is given by

$$\theta_{EL} = \sin^{-1}\left(\frac{R_e}{R_s}\sin\left(R/R_e\right)\right). \tag{5}$$

Notice that both the grazing angle ψ and the elevation angle θ_{EL} are range dependent.

From Fig. 1 we also have

$$\theta_{EL} = \sin^{-1}\left(\frac{1}{1 + H/R_e}\cos\psi\right). \tag{6}$$

Similarly from the triangle ACD we obtain the alternate formula

$$\theta_{EL} = \pi/2 - \theta_e - \psi = \pi/2 - \psi - R/R_e \tag{7}$$

for the elevation angle as well. The slant range, grazing angle and elevation angle as functions of range are shown in Fig. 3 and Fig. 4.

2.2 Maximum Range on Earth

The curvature of earth limits the maximum range achievable by a satellite located at height H as shown in Fig. 5.

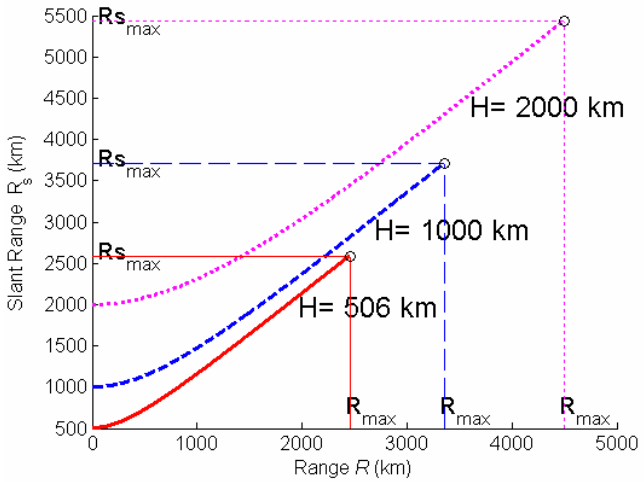

Figure 3. Slant range *vs.* range

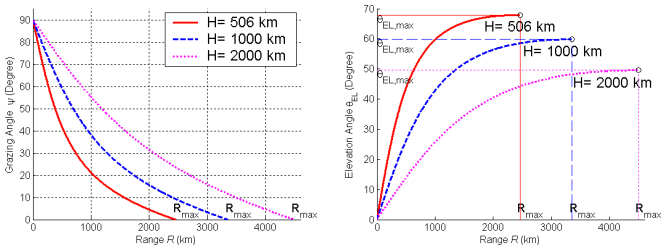

Figure 4. Grazing angle and elevation angle *vs.* range.

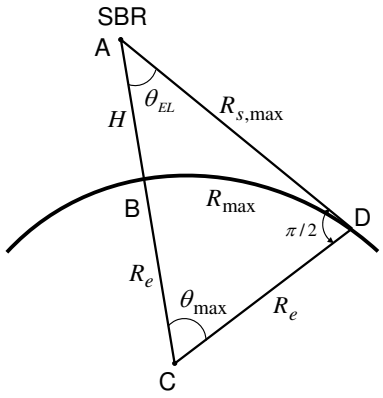

Figure 5. Maximum range on ground.

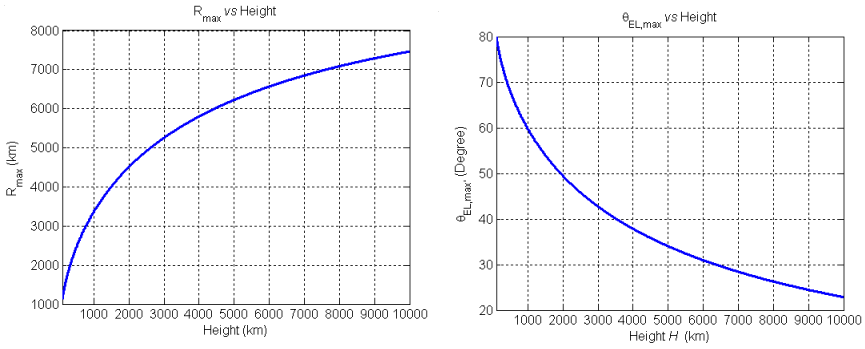

Figure 6. Maximum range and elevation angle *vs.* satellite height.

At maximum range, the slant range becomes tangential to the earth so that the grazing angle $\psi = 0$ and from Fig. 5

$$\theta_{\max} = \cos^{-1}\left(\frac{1}{1+H/R_e}\right). \tag{8}$$

The maximum range on earth for an SBR located at height H is given by

$$R_{\max} = R_e\,\theta_{\max} = R_e\cos^{-1}\left(\frac{1}{1+H/R_e}\right). \tag{9}$$

Similarly maximum slant range at the same height is given by

$$R_{s,\max} = (R_e + H)\sin\left\{\cos^{-1}\left(\frac{1}{1+H/R_e}\right)\right\}, \tag{10}$$

and the maximum elevation angle equals

$$\theta_{EL,\max} = \frac{\pi}{2} - \theta_{\max} = \frac{\pi}{2} - \cos^{-1}\left(\frac{1}{1+H/R_e}\right). \tag{11}$$

For a low-earth orbit (LEO) satellite located at 506 km above the ground, the maximum range is 2,460 km and $\theta_{EL,\max} = 67.9^o$.

2.3 Mainbeam Footprint Size

The mainbeam of the radar generates a footprint on the ground whose size will depend upon the actual range R. Let ϕ_{EL} represent the mainbeam width of the antenna pattern in the elevation plane. Further, let R_T and R_H denote the ranges of the 'toe' and 'heel' of the mainbeam footprint whose center is at range R, as shown in Fig. 7. Further, let ψ_T

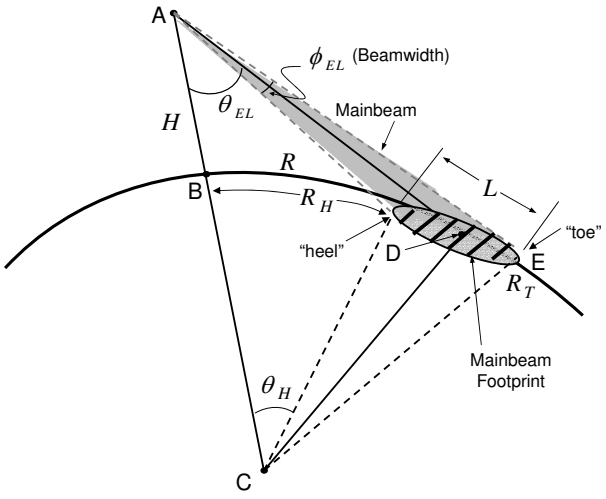

Figure 7. Mainbeam footprint at range R. Distances R_T and R_H correspond to ranges at the 'toe' and 'heel' of the footprint. Range R represents the curved distance BD to the center of the footprint.

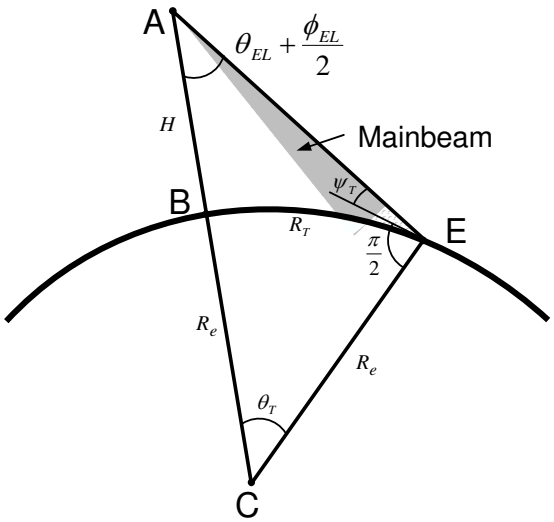

Figure 8. Range calculation at the 'toe' of the mainbeam footprint.

and ψ_H represent the grazing angles at the 'toe' and 'heel' of the mainbeam footprint. Thus, from triangle ACE in Fig. 8 that corresponds to the footprint 'toe', we have

$$\frac{\sin(\pi/2+\psi_T)}{R_e+H} = \frac{\sin(\theta_{EL}+\phi_{EL}/2)}{R_e} \tag{12}$$

where θ_{EL} represents the elevation at range R. This gives the grazing angle at the 'toe' to be

$$\psi_T = \cos^{-1}\left\{\left(1+\frac{H}{R_e}\right)\sin\left(\theta_{EL}+\frac{\phi_{EL}}{2}\right)\right\}, \tag{13}$$

and similarly the grazing angle at the 'heel' is given by

$$\psi_H = \cos^{-1}\left\{\left(1+\frac{H}{R_e}\right)\sin\left(\theta_{EL}-\frac{\phi_{EL}}{2}\right)\right\}. \tag{14}$$

Also, from Fig. 8, the core angle at the center of earth for the 'toe' equals

$$\theta_T = \frac{\pi}{2} - \theta_{EL} - \frac{\phi_{EL}}{2} - \psi_T \tag{15}$$

and the range to the mainbeam 'toe' equals

$$R_T = R_e\theta_T = R_e\left(\frac{\pi}{2} - \theta_{EL} - \frac{\phi_{EL}}{2} - \psi_T\right). \tag{16}$$

Similarly, the range to the 'heel' of the mainbeam equals

$$R_H = R_e\theta_H = R_e\left(\frac{\pi}{2} - \theta_{EL} + \frac{\phi_{EL}}{2} - \psi_H\right). \tag{17}$$

This gives the length of the footprint of the mainbeam at range R to be

$$L = R_T - R_H = R_e(\psi_H - \psi_T - \phi_{EL}). \tag{18}$$

Let ψ_{AZ} represents the beamwidth in the azimuth direction. Then the horizontal mainbeam beamwidth equals

$$W = R_s\,\phi_{AZ}. \tag{19}$$

As Fig. 9 shows, both the length and width of the footprint are functions of range and height. In summary, when the antenna mainbeam is focused along θ_{EL}, returns from the illuminated region of the corresponding mainbeam footprint will contribute toward clutter from that range [5].

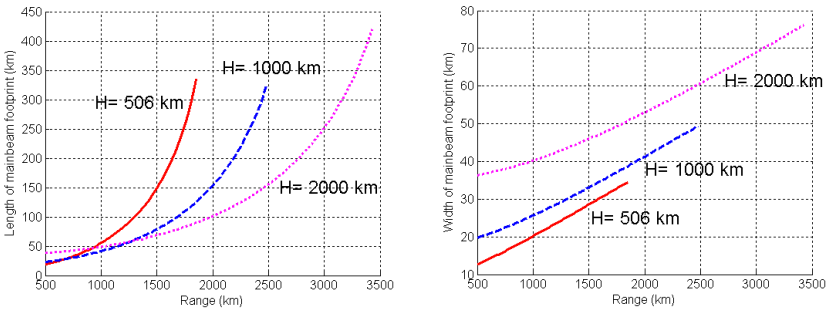

Figure 9. (a) Length and (b) width of mainbeam footprint *vs.* range. Mainbeam beamwidths in both elevation and azimuth directions are assumed to be 1^o.

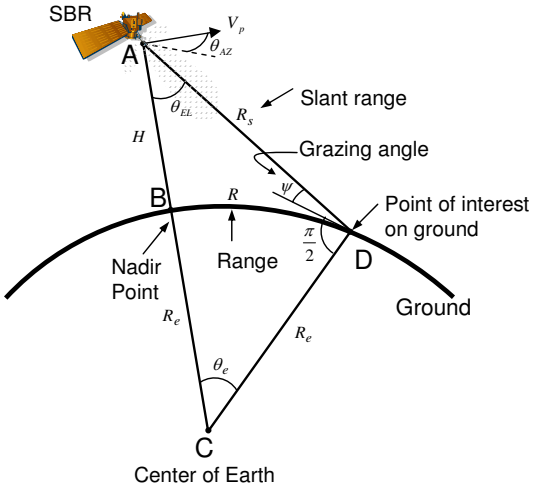

Figure 10. Parameters of an SBR pointing its mainbeam to a ground point D.

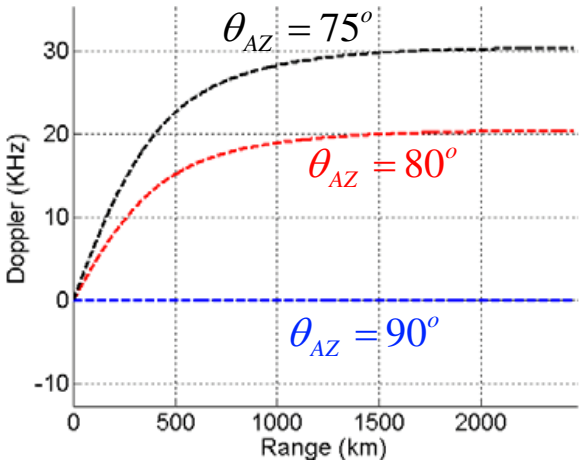

Figure 11. Doppler dependency on range *vs.* azimuth angle.

2.4 Doppler Shift

Consider a space based radar (SBR) at height H above the earth on a great circular orbit that is inclined at an angle η_i (with respect to the equator). By virtue of earth's gravity the SBR is moving with velocity

$$V_p = \sqrt{GM_e/(R_e + H)} \tag{20}$$

in a circular orbit and this contributes to a relative velocity of

$$V_p \cos\theta_{AZ} \sin\theta_{EL} \tag{21}$$

along the line-of-sight for a point of interest D on the ground that is at an azimuth angle θ_{AZ} with respect to the flight path and an elevation angle θ_{EL} with respect to the nadir line as shown in Fig. 10.

If T_r represents the radar pulse repetition rate and λ the operating wavelength, then the Doppler ω_d contributed by (21) equals [1, 7, 11, 12].

$$\omega_d = \frac{2V_pT_r}{\lambda/2} \sin\theta_{EL} \cos\theta_{AZ} \tag{22}$$

and (22) accounts for the Doppler frequency of the ground return due to the SBR motion. Fig. 11 shows the Doppler dependency on range as a function of the azimuth angle. Clearly for a given azimuth angle, the difference in Doppler along the range is minimum (zero) when the azimuth look direction coincides with the bore-side of the array $\theta_{AZ} = \pi/2$. If the earth's rotation is included as we shall see in section 3.2,

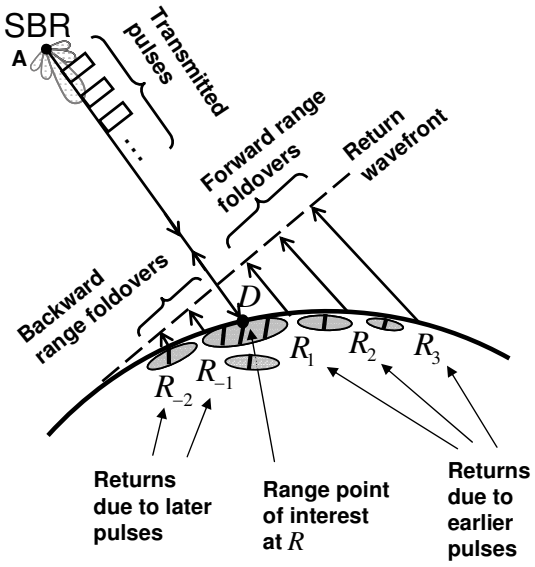

Figure 12. Common wavefront showing all range ambiguity returns corresponding to a point of interest at range R.

the Doppler difference due to range generates an undesirable 'Doppler filling' effect when data samples from different range bins are used to estimate the covariance matrix.

3. Range Foldover and Earth's Rotation

3.1 Range Foldover Phenomenon

To detect targets, the radar transmits pulses periodically. Range foldover occurs when clutter returns from previously transmitted pulses, returning from farther range bins, are combined with returns from the point of interest. Depending on the size of the mainbeam footprint, the 2-D antenna array pattern and the radar pulse repetition frequency, range foldover can occur both from within the mainbeam as well as from the entire 2-D region. The effect of mainbeam foldover is discussed first, followed by its extension to the entire 2-D region [1, 3].

Range Resolution. Let τ represent the *output* pulse length and T_r the pulse repetition interval. Pulses travel along the slant range and interact with the ground through the mainbeam as well as the sidelobes of the antenna array as shown in Fig. 13.

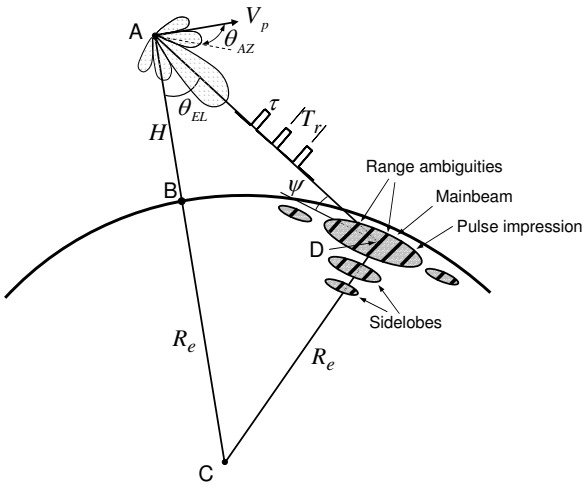

Figure 13. Mainbeam range ambiguities.

Each pulse travels along the slant range and hence the slant range that can be recovered unambiguously is of size $\frac{c\tau}{2}$. Thus, slant range resolution is given by

$$\delta_{SR} = \frac{c\tau}{2}. \tag{23}$$

Translating to the ground plane, since the pulse wavefront is perpendicular to the slant range direction, we get the range resolution on the ground to be

$$\delta_R = \frac{c\tau}{2\cos\psi} = \frac{c\tau}{2}\sec\psi. \tag{24}$$

Thus δ_R represents the ground-plane spatial resolution achievable by the SBR. Two objects that are separated by a distance less than δ_R will be indistinguishable by the radar. Notice that only the *output* pulse length contributes to the range resolution and it can be orders of magnitude smaller than the actual pulse length because of pulse compression effects. For example, using chirp waveforms it is possible to realize 1:100 or higher order compression. From (24) for short range regions where the grazing ψ is closer to $\pi/2$, the range resolution is very poor, and for long range the resolution approaches its limiting value δ_{SR} as $\psi \to 0$.

Total Range Foldover. Radar transmits pulses every T_r seconds and for high PRF situations, following (24), the distance Δ_R between range ambiguities on the ground (distance between consecutive pulse

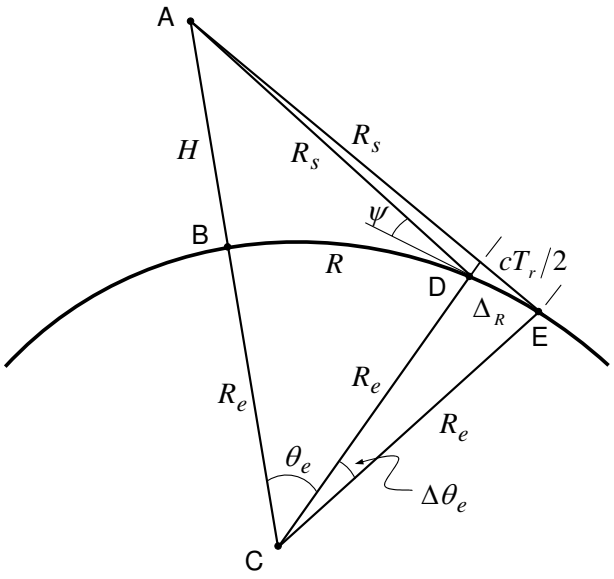

Figure 14. Distance between range ambiguities.

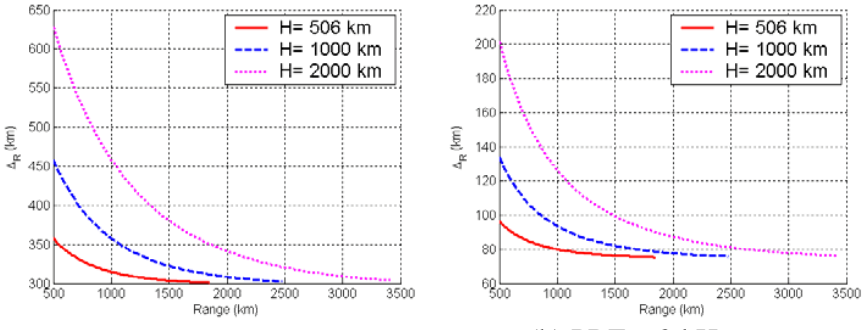

Figure 15. Δ_R *vs.* range for (a) $PRF = 500$ Hz and (b) 2 kHz.

shadows) is given by

$$\Delta_R = \frac{cT_r}{2} \sec \psi. \tag{25}$$

Equation (25) assumes a high PRF situation where the grazing angles at various range ambiguities are assumed to be equal. The general situation that takes the change in grazing angle into account is shown in Fig. 14.

If R_s represents the slant range at the end of one pulse (say at D), $R_s + cT_r/2$ is the new slant range at the end of the next pulse at E. Let

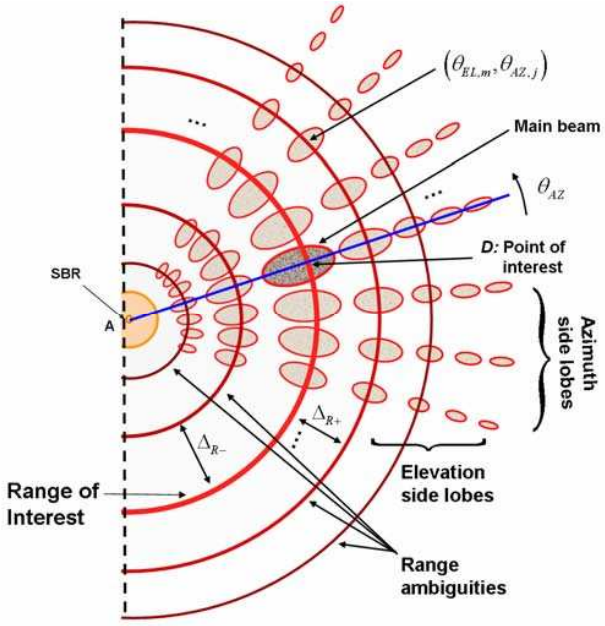

Figure 16. 'Range foldover' phenomenon.

$R_1 = R + \Delta_R$ represent the new range corresponding to the second pulse shadow on the ground at E. From triangle ACE in Fig. 14

$$(R_s + cT_r/2)^2 = R_e^2 + (R_e + H)^2 - 2R_e(R_e + H)\cos\left(\frac{R + \Delta_R}{R_e}\right) \quad (26)$$

or

$$\Delta_R = R_e \cos^{-1}\left(\frac{R_e^2 + (R_e + H)^2 - (R_s + cT_r/2)^2}{2R_e(R_e + H)}\right) - R. \quad (27)$$

From Fig. 15, interestingly Δ_R is a decreasing function of R, and when R is relatively small, the distance between the pulse shadows on the ground is large and is seen to decrease as R increases. However, for large values of range, Δ_R remains constant at its limiting $cT_r/2$. This also follows from (25) since for large R the grazing angle approaches zero.

To compute the total number of range foldovers for the entire range, we can make use of Fig. 16. In Fig. 16, the point of interest (D) is within the mainbeam, and the return of the radar pulse from there represents the main clutter. However because of the 2-D antenna pattern, previous pulse returns returning from adjacent 'range ambiguities points' — both

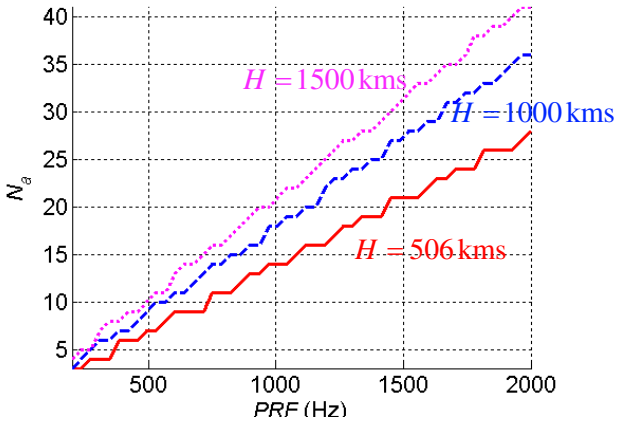

Figure 17. Number of range ambiguities as a function of SBR height and *PRF*.

forward and backward — that have been appropriately scaled by the array gain pattern get added to the mainbeam return causing additional range foldover.

To compute the immediate forward and backward range ambiguity points (E and F respectively), the geometry in Fig. 14 can be used. In general, the k^{th} forward and backward range ambiguity points are given by

$$R_{\pm k} = R_e \cos^{-1}\left(\frac{R_e^2 + (R_e + H)^2 - (R_s \pm kcT_r/2)^2}{2R_e(R_e + H)}\right), \quad k = 1,\ 2,\ \ldots$$

where $R_{+k} = R_k$. Fig. 12 shows the return wavefront from all range ambiguities corresponding to a point of interest D at range R.

Let N_a refer to the total number of range ambiguities (both forward and backward) corresponding to a range bin of interest. The clutter returns from forward and backward range ambiguities get scaled by the array gain corresponding to those locations and get added to the returns from the point of interest. Fig. 17 shows the total number of range ambiguities in the 2D region as a function of SBR height and *PRF*. From this figure, it is seen that the total number of range foldovers at 500Hz *PRF* is 7. Returns from the N_a range ambiguities contribute to the clutter at this particular range [1–3, 8].

3.2 Modeling Earth's Rotation for SBR

As we have seen in Section 3.1 the range foldover phenomenon — clutter returns that correspond to previous radar pulses — contributes to the SBR clutter. Another important phenomenon that affects the

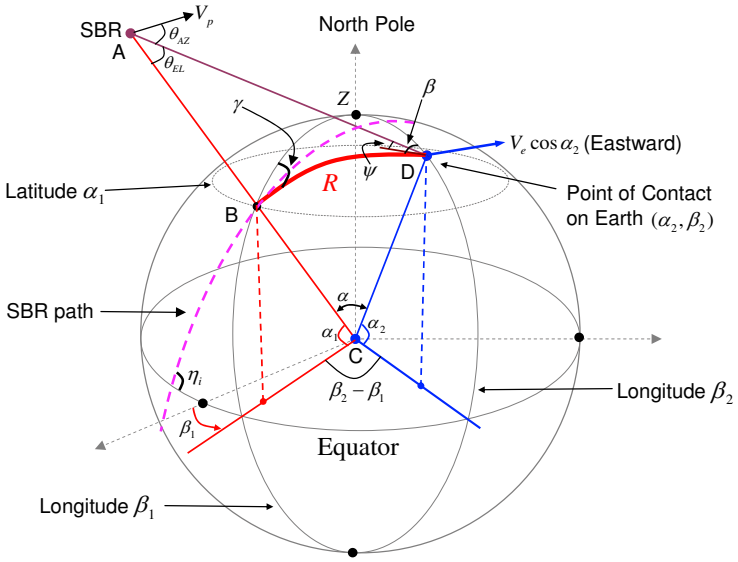

Figure 18. Doppler contributions from SBR velocity and earth rotation.

clutter data is the effect of earth's motion around its own axis. At various locations on earth this contributes differently to Doppler, and the effect is modeled here [1, 9].

For any point on earth at range R that is at elevation angle θ_{EL} and azimuth angle θ_{AZ} from an SBR at height H, the conventional Doppler shift relative to the SBR equals [5]

$$\omega_d = \frac{2V_pT_r}{\lambda/2} \sin\theta_{EL} \cos\theta_{AZ}, \tag{28}$$

as derived in Section 2.4. Let η_i denote the inclination of the SBR orbit with respect to the equator (see Fig. 18–Fig. 19).

As the SBR moves around the earth, the earth itself is rotating around its own axis on a 23.9345 hour basis in a west-to-east direction. This contributes an eastward motion with equatorial velocity of

$$V_e = \frac{2\pi R_e}{23.9345 \times 3600} = 0.4651\,\text{km/sec} \tag{29}$$

Let (α_1, β_1) refer to the latitude and longitude of the SBR nadir point B and (α_2, β_2) those of the point of interest D as shown in Fig. 18–Fig. 19.

As a result, the point of interest D on the earth at latitude α_2 rotates eastward with velocity $V_e \cos\alpha_2$, which will contribute to the Doppler

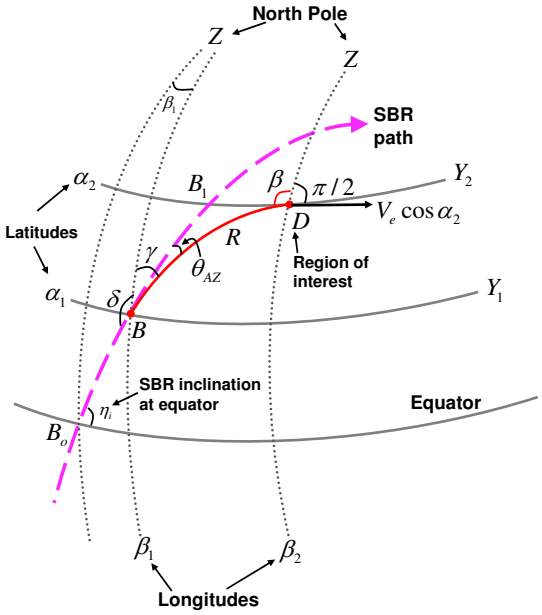

Figure 19. Effect of earth rotation on Doppler frequency.

in (22) as well. To compute this new component in Doppler shift, note from Fig. 19 that the angle BDY_2 between the ground range vector R and the earth velocity vector at D equals $(\pi/2+\beta)$ so that [5]

$$V_o = V_e \cos\alpha_2 \cos(\pi/2+\beta) = -V_e \cos\alpha_2 \sin\beta \tag{30}$$

represents the earth's relative velocity at D along the ground range direction towards B. Since the grazing angle represents the slant range angle with respect to the ground range at D (see Fig. 18), we have

$$V_o \cos\psi = -V_e \cos\alpha_2 \sin\beta \ \cos\psi \tag{31}$$

represents the relative velocity contribution between the SBR and the point of interest D due to the earth's rotation towards the SBR. Combining (21) and (31) as in (22), we obtain the modified Doppler frequency that also accounts for the earth's rotation to be

$$\omega_d = \frac{2T_r}{\lambda/2}\left(V_p \sin\theta_{EL}\cos\theta_{AZ} - V_e \cos\alpha_2 \sin\beta\cos\psi\right) \tag{32}$$

After some simplification, we obtain the modified Doppler frequency to be [11, 12]

$$\omega_d \ = \frac{2V_pT_r}{\lambda/2}\rho_c \sin\theta_{EL} \ \cos(\theta_{AZ}+\phi_c), \tag{33}$$

where

$$\phi_c = \tan^{-1}\left(\frac{\Delta\sqrt{\cos^2\alpha_1 - \cos^2\eta_i}}{1 - \Delta\cos\eta_i}\right) \tag{34}$$

and

$$\rho_c = \sqrt{1 + \Delta^2\cos^2\alpha_1 - 2\Delta\cos\eta_i}. \tag{35}$$

In (33)–(35), ϕ_c represents the crab angle and ρ_c represents the crab magnitude. In summary, the effect of earth's rotation on the Doppler velocity is to introduce a crab angle and crab magnitude into the SBR azimuth angle and modify it accordingly [1, 11, 12]. Interestingly both these quantities depend only on the SBR orbit inclination and its latitude, and *not* on the latitude or longitude of the clutter patch of interest.

Equation (33) corresponds to the case where the region of interest D is to the east of the SBR path as shown in Fig. 19. If, on the other hand, the region of interest is to the west of the SBR path, then

$$\omega_d = \frac{2V_pT_r}{\lambda/2}\rho_c\sin\theta_{EL}\ \cos(\theta_{AZ} - \phi_c) \tag{36}$$

with ϕ_c, ρ_c as defined in (33)–(35). Combining (33) and (36), we obtain the modified Doppler to be

$$\omega_d = \frac{2V_pT_r}{\lambda/2}\rho_c\sin\theta_{EL}\ \cos(\theta_{AZ} \pm \phi_c). \tag{37}$$

In (37), the plus sign is to be used when the region of interest is to the east of the SBR path and the minus sign is to be used when the point of interest is to the west of the SBR path.

Fig. 20 shows the crab angle and crab magnitude as a function of SBR latitude for different inclination angles. Once again about 3.77^o error can be expected for the crab angle in the worst case.

The effect of crab angle on Doppler as a function of azimuth angle for various range values is shown in Fig. 21. As (33) shows, the effect of earth's rotation is to shift the azimuth angle appearing in the Doppler by approximately $\phi_c = 3.77^o$ and simultaneously modify the Doppler magnitude as well. As a result, even for $\theta_{AZ} = 90^o$, the Doppler peak values occur away from $\omega_d = 0$ depending on the range. This shift in Doppler with and without the crab effect is illustrated in Fig. 21 for various azimuth angles.

4. Application of STAP for SBR

In this section, SBR data modeling is first carried out with appropriate Doppler parameters. By considering the two phenomena, with and

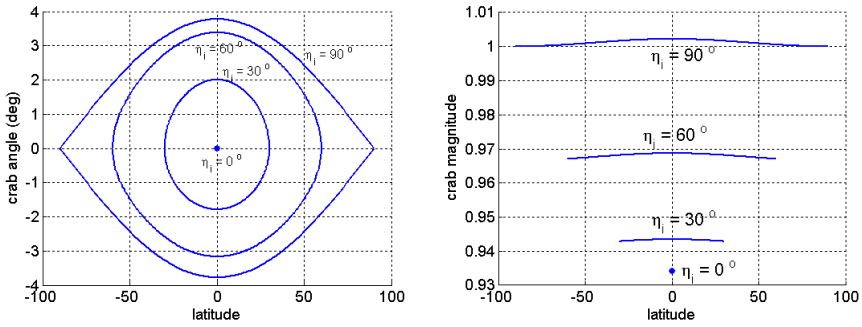

Figure 20. (a) Crab angle and (b) crab magnitude as functions of SBR latitude for different inclination angles.

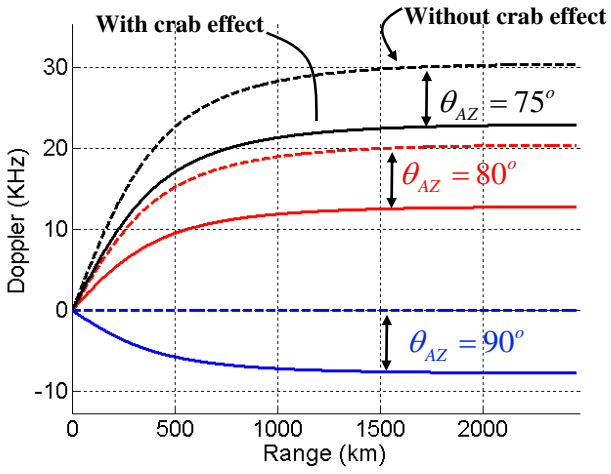

Figure 21. Effect of crab angle on range-Doppler profile.

without range foldover effect and with and without earth's rotational effect — four cases of interest can be generated.

4.1 SBR Data Modeling

Consider an SBR array with N sensors and M pulses. If the incoming wavefront makes an azimuth angle θ_{AZ} and elevation angle θ_{EL} with reference to the array, define the first sensor output to be $x_1(t)$ and

$$c = \sin\theta_{EL}\cos\theta_{AZ} \tag{38}$$

represent the 'cone angle' associated with the spatial point θ_{EL}, θ_{AZ} for the SBR array. Then the concatenated data vector due to the N sensors and M pulses is the MN by 1 vector given by [12]

$$\mathbf{x}(t) = \mathbf{s}(c, \omega_d)\, x_1(t), \tag{39}$$

where

$$\mathbf{s}(c, \omega_d) = \mathbf{b}(\omega_d) \otimes \mathbf{a}(c) \tag{40}$$

represents the spatial-temporal steering vector with $\otimes$ representing the Kronecker product. $\mathbf{a}(c)$ in (40) represents the spatial steering vector and is given by

$$\mathbf{a}(c) = \left[1, e^{-j\pi dc}, e^{-j2\pi dc}, \cdots, e^{-j(N-1)\pi dc}\right]^T \tag{41}$$

$\mathbf{b}(\omega_d)$ in (40) represents the temporal steering vector given by

$$b(\omega_d) + \left[1, e^{-j\pi\omega_d}, e^{-j2\pi\omega_d}, \cdots, e^{-j(M-1)\pi\omega_d}\right]^T \tag{42}$$

Let $\theta_{AZ_j} = \theta_{AZ} + i\Delta\theta,\ i = 0,\ \pm 1,\ \pm 2,\ \pm N_o$ represent the azimuth angles associated with the field of view, and $\theta_{EL_m},\ m = 0, 1, 2, \cdots, N_a$ the elevation angles corresponding to the total number of range foldover in the field of view. Further let

$$c_{m,\,i} = \sin\theta_{EL\,m}\cos\theta_{AZ_i} \tag{43}$$

represent the cone angle associated with the location $\theta_{EL_m}, \theta_{AZ_i}$. The total clutter return represents various range foldover returns that span over all azimuth angles. This gives the ensemble average clutter covariance matrix associated with range r_k to be

$$\mathbf{R}_k = E\left\{\mathbf{y}_k \mathbf{y}_k^*\right\} \tag{44}$$

where $\mathbf{y}_k$ represents the clutter data.

4.2 SINR With/Without Earth's Rotation and Range Foldover

In practice, the covariance matrix in (44) corresponding to range r_k is unknown and needs to be estimated from data using the expression

$$\hat{\mathbf{R}}_k = \sum_j \mathbf{x}_{k+j}\mathbf{x}_{k+j}^*. \tag{45}$$

In (45) the number of range bins over which the summation is carried out is chosen so as to maintain stationary behavior for $\hat{\mathbf{R}}_k$. The estimated adaptive weight vector corresponding to (45) is given by the sample matrix inversion (SMI) method as

$$\hat{\mathbf{w}}_k = \hat{\mathbf{R}}_k^{-1}\,\mathbf{s}(c_t,\,\omega_{d_t})\;. \tag{46}$$

A useful way of evaluating the performance of a particular STAP algorithm is the signal power to interference plus noise ratio (SINR) defined by

$$SINR = \frac{|\mathbf{w}^*\,\mathbf{s}|^2}{\mathbf{w}^*\,\mathbf{R}\,\mathbf{w}} \tag{47}$$

where $\mathbf{w}$ is the estimated adaptive weight vector and $\mathbf{R}$ is the ideal clutter plus noise covariance matrix defined in (44). For the SMI, (47) can be written as

$$SINR = \frac{|(s)^*\,\hat{\mathbf{R}}^{-1}\,(s)|^2}{(s)^*\,\hat{\mathbf{R}}^{-1}\,R\,\hat{\mathbf{R}}^{-1}(s)} \tag{48}$$

Clearly the performance of (48) is bounded by the ideal matched filter output $SINR_{ideal}$ obtained by letting $\hat{\mathbf{R}} = \mathbf{R}$ in (44). This gives

$$SINR_{ideal} = \mathbf{s}^*(c,\,\omega_d)\,\mathbf{R}^{-1}\,\mathbf{s}(c,\,\omega_d) \tag{49}$$

where $\mathbf{s}(c,\omega_d)$ is given by (40) and represents the space time steering vector for the desired point of interest located at $\theta = (\theta_{EL}, \theta_{AZ})$ that corresponds to the cone-angle

$$c = \sin\theta_{EL}\cos\theta_{AZ}, \tag{50}$$

and Doppler frequency ω_d for the SBR configuration under consideration. To quantify the performance deterioration due to earth's rotation and range foldover, the following four situations corresponding to four different clutter covariance matrices are identified:

1 No range foldover, no earth's rotation (ideal case);

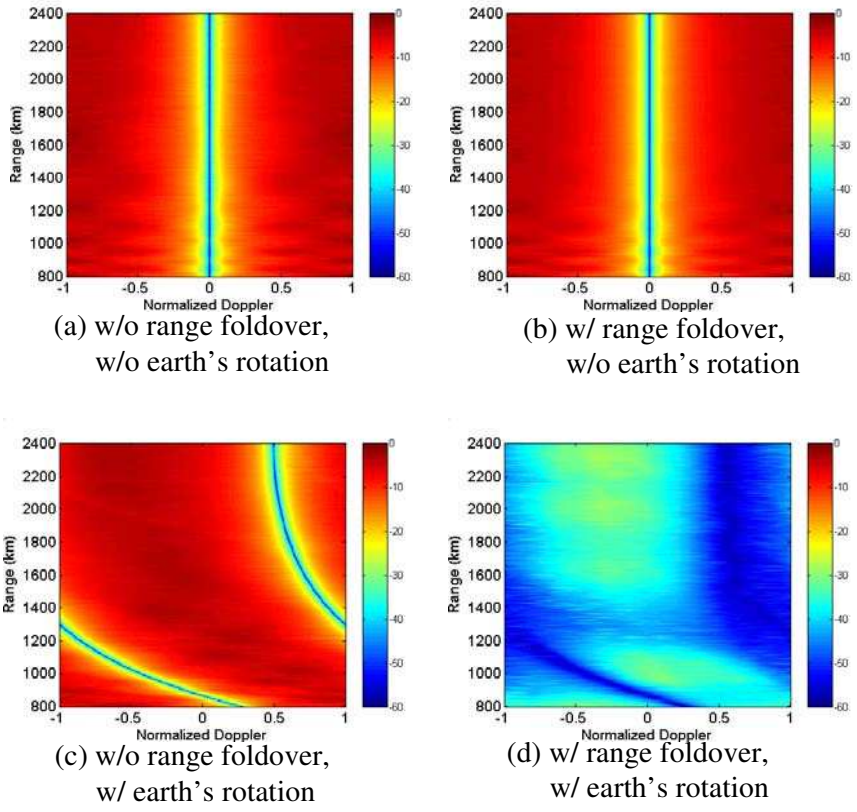

Figure 22. SINR loss with/without range foldover and earth's rotation as a function of range and Doppler

2 Range foldover present, no earth's rotation;

3 No range foldover, earth's rotation present;

4 Range foldover present, earth's rotation present.

Fig. 22 shows the SINR loss for the four cases above as a function of range and Doppler for an SBR located at height 506 km above the ground. The PRF is 500 Hz and $\theta_{AZ} = 90^o$. The output is normalized with respect to the noise only case. The performance is significantly degraded when both range foldover and earth's rotation are present at the same time.

Fig. 23 shows the SINR loss for two different ranges. The SINR loss is on the order of 20–40 dB when both range foldover and earth's rotation are present, depending on the actual range. The performance in terms of clutter nulling is inferior when these two effects are present.

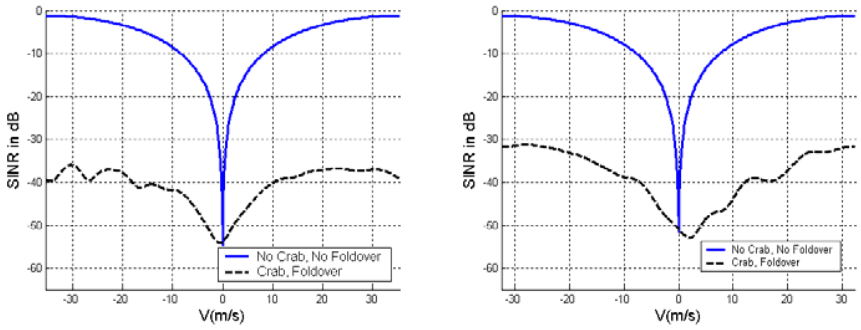

Figure 23. SINR loss with/without range foldover and earth's rotation for (a) 900 km and (b) 2000 km ranges.

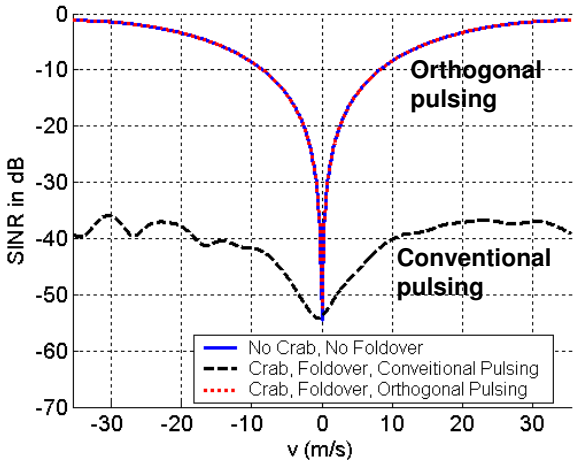

Figure 24. SINR improvement using orthogonal pulsing, range=900 kms

Thus, having both range foldover and earth's rotation at the same time results in unacceptable performance degradation as shown in Fig. 23; whereas when either one is present separately, the effect can be rectified.

5. Orthogonal Pulsing Scheme

Waveform diversity can be used on the sequence of transmitted radar pulses to realize the above goal by suppressing the range foldover returns. In ordinary practice, a set of identical pulses are transmitted. To suppress returns due to range foldover, for example, individual pulses

$f_1(t),\ f_2(t),\ \cdots$ can be made orthogonal to each other so that

$$\int_o^{T_o} f_i(t) f_l(t)\, dt = \delta_{i,l}, \quad i,\, l = 1,\ 2,\ \cdots,\ N_a, \tag{51}$$

where N_a is the maximum number of distinct range foldovers present in the data and $\delta_{i,l}$ is the Kronecker delta. Then, with appropriate matched filtering [13], the range ambiguous returns can be minimized from the main return corresponding to the range of interest. Note that for range foldover elimination, waveform diversity needs to be implemented only over N_a pulses. For an SBR located at a height of 506 km and an operating PRF = 500 Hz, $N_a \approx 7$. This is the case since matched filtering will eliminate the superimposed range foldover returns since they correspond to waveforms that are orthogonal to the one in the mainbeam. Fig. 24 shows the SINR improvement using eight orthogonal waveforms [13]. The performance is restored to the ideal case when orthogonal waveforms are used.

In summary, using waveform diversity on transmit, it is possible to eliminate the effect of range foldover resulting in performance improvement as shown in Fig. 24. The resulting performance will be approximately the same as the performance shown in Fig. 22 (a), indicating that using waveform diversity on transmit, it is possible to achieve performance close to the ideal case even in the presence of both range foldover and earth's rotation. The results presented here correspond to the case where the ensemble averaged clutter covariance matrix is given. The case where the covariance matrix is estimated from secondary data is more challenging.

References

[1] K. Y. Li *et. al.*, STAP for Space Based Radar *Air Force Research Laboratory Final Technical Report*, AFRL-SN-RS-TR-2004-170, June 2004.

[2] Mark E. Davis and Braham Himed, L Band Wide Area Surveillance Radar Design Alternatives, *International Radar 2003 — Australia*, September 2003.

[3] Mark E. Davis, Braham Himed, and David Zasada, Design of Large Space Radar for Multimode Surveillance, *IEEE Radar Conference*, Huntsville, AL, pp. 1–6, May 2003.

[4] John Maher, Mark E. Davis, Robert J. Hancock, and Sidney W. Theis, High Fidelity Modeling of Space-Based Radar, *2003 IEEE Radar Conference*, Huntsville, AL, pp. 185–191, May 2003.

[5] Leopold J. Cantafio, *Space-Based Radar Handbook* Artech House, Boston, 1989.

[6] Troy L. Hacker, Performance Analysis of a Space-Based GMTI Radar System Using Separated Spacecraft Interferometry MS Thesis, Department of Aeronautics and Astronautics *Massachusetts Institute of Technology*, Lexington, MA, May 2000.

[7] J. R. Guerci, *Space-Time Adaptive Processing for Radar* Artech House, Boston, 2003.

[8] S.M. Kogon, D.J. Rabideau, R.M. Barnes, Clutter Mitigation Techniques for Space-Based Radar, *IEEE International Conference on Radar*, Vol. 4, pp. 2323–2326 March 1999.

[9] Peter Zulch, Mark Davis, Larry Adzima, Robert Hancock, Sid Theis, The Earth Rotation Effect on a LEO L-Band GMTI SBR and Mitigation Strategies, *IEEE Radar Conference*, Philadelphia, PA, April 2004.

[10] G.A. Andrews and K. Gerlach, SBR Clutter and Interference', Ch. 11, *Space-Based Radar Handbook*, Ed. Leopold J. Cantafio, Artech House, Boston, 1989.

[11] S. U. Pillai, B. Himed, K. Y. Li, Waveform Diversity for Space Based Radar, *Proc. of Waveform Diversity and Design*, Edinburgh, Scotland, Nov 8–10, 2004.

[12] S. U. Pillai, B. Himed, K. Y. Li, Modeling Earth's Rotation for Space Based Radar, *Asilomar Conference on Signals, Systems, and Computer*, Pacific Grove, CA, Nov 7–10, 2004.

[13] S. U. Pillai, B. Himed, K. Y. Li, Orthogonal Pulsing Schemes for Improved Target Detection in Space Based Radar, *2005 IEEE Aerospace Conference*, Big Sky, MT, March 5–12, 2005.